IPN Progress Report 42-207 • November 15, 2016

RF/Optical Demonstration: Focal Plane Assembly

Daniel J. Hoppe,* Sang Chung,† Joe Kovalik,‡ Eric Gama,*
and Michela Munoz Fernandez▲

ABSTRACT. — In this article, we describe the second-generation focal plane optical assembly employed in the RF/optical demonstration at DSS-13. This assembly receives reflected light from the two mirror segments mounted on the RF primary. The focal plane assembly contains a fast steering mirror (FSM) to stabilize the focal plane spot, a pupil camera to aid in aligning the two segments, and several additional cameras for receiving the optical signal prior to as well as after the FSM loop.

I. Introduction

Future plans for deep-space communication are centered around optical communications. Optical communications offer the promise of increased bandwidth as well as reduced mass and volume requirements on the spacecraft when compared to RF systems [1]. Details on the latest spacecraft optical terminal can be found in [2]. The ground segment of the optical link is as important as the spacecraft terminal and somewhat less work has been done in this area. Several ground terminal concepts are described in [3,4]. The most up-to-date assessment of the cost and performance of the ground side of optical communications systems is described in [5–8]. It is almost certain that while an optical channel will be used to provide high-volume downlink from the spacecraft, uplink commanding and emergency communications will certainly use RF channels. This has led to the consideration of hybrid RF/optical ground stations [9]. Recently, the performance of open-air gamma-ray observatories for optical communications has also been studied [10].

In its basic configuration, the ground station must contend with atmospheric turbulence, which limits the achievable spot size for the received signal in the focal plane. This in turn limits the sky or planet noise entering the detector. Thus, diffraction-limited operation is not a requirement for the ground station, but rather the mirror surface, segment control, and pointing errors of the terminal need to be kept small when compared to the turbulence. This brings up the possibility of admitting low-cost, open-air ground stations into the design space along with more conventional approaches similar to dome-based astronomi-

* Communications Ground Systems Section.
† Communications Architectures and Research Section.
‡ Flight Communications Section.
▲ Mission Control Systems Section.

The research described in this publication was carried out by the Jet Propulsion Laboratory, California Institute of Technology, under a contract with the National Aeronautics and Space Administration.

cal telescopes. An experimental system to demonstrate and quantify the key performance characteristics of an open-air ground station with RF quality structure and pointing has been assembled at Deep Space Station (DSS)-13, a 34-m-diameter RF antenna at Goldstone, California [11], depicted in Figure 1.

Figure 1. DSS-13 34-m beam-waveguide antenna.

Figure 2 depicts the two major subassemblies making up the demonstrator. A pair of spherical glass segments are mounted through the RF panels directly to the antenna backup structure and a focal plane assembly, camera box, is mounted off the RF secondary. Light incident on the segments is focused in the vicinity of the camera box and detected using off-the-shelf imaging cameras. Astronomical sources are tracked using the RF pointing and tracking system, and the segments are actively pointed to maintain a minimum composite spot size in the focal plane.

Figure 3 shows a photograph of the assembly on the RF primary. The enclosure assembly has dimensions measuring approximately 38.5″ × 36″ × 20″. The overall weight of the assembly is approximately 250 lb. Two 35-cm hexagonal segments are mounted inside the enclosure. The segments have a spherical figure with a focal length of approximately 12 m. Five actuators control the segments, with three controlling the tip, tilt, and piston of the pair, while two control tip/tilt of one segment relative to the other. The segment positions are actively controlled throughout a given observation to compensate for RF structural deformations and RF pointing/tracking errors. In the lower center portion of the photo, a telescope that is aligned with the RF pointing direction is visible. Since its field of view is large compared to that of the two-segment system, it can be used as an acquisition aid. In practice, the RF pointing accuracy and repeatability have been sufficient and the image from this telescope

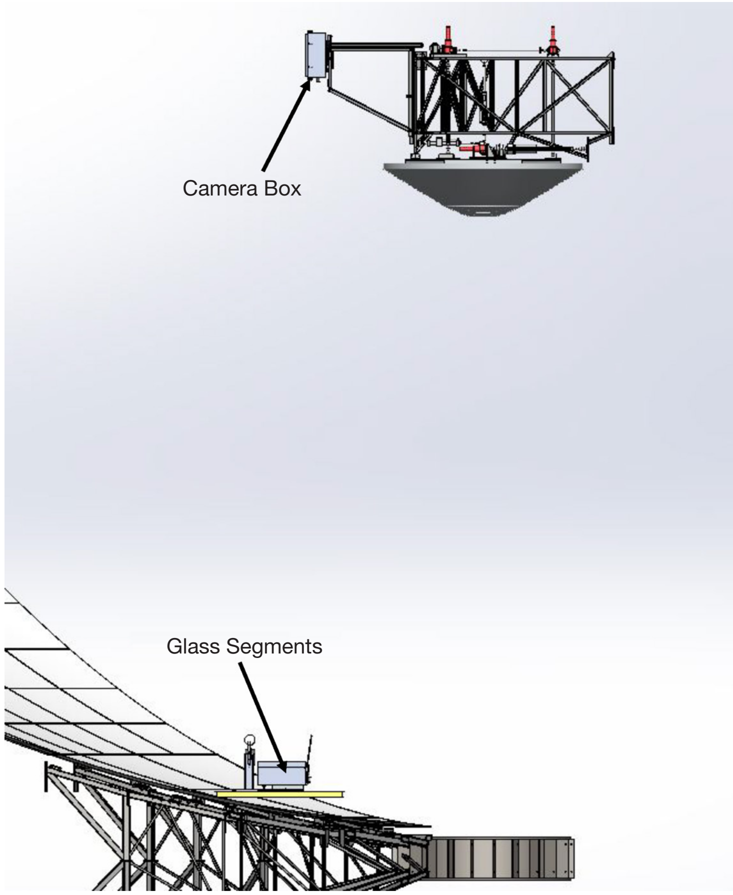

Figure 2. 3D model of the RF/optical demonstration.

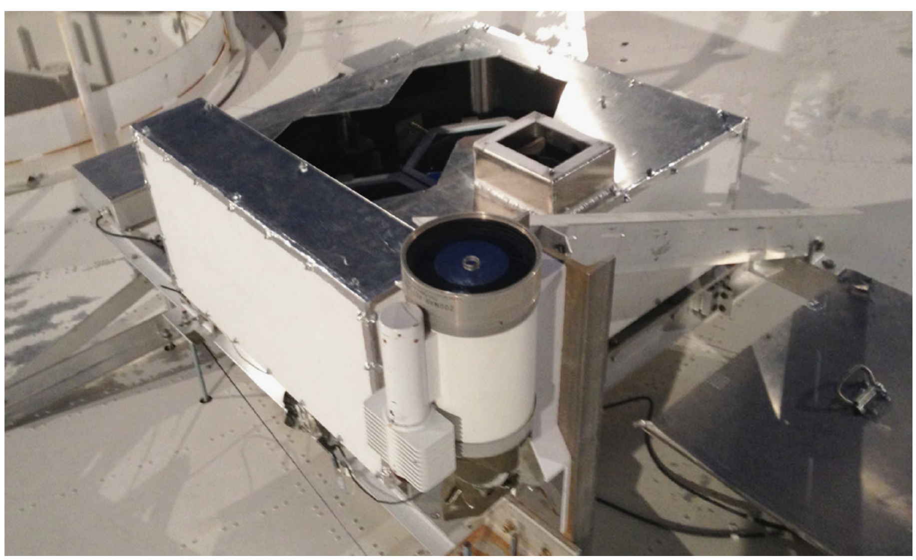

Figure 3. Optical segments inside the enclosure on the RF primary surface.

is rarely used. One additional camera, mounted on the tip/tilt/piston portion of the mirror assembly, views a small light-emitting diode (LED) source mounted on the front of the camera box. The square aperture slightly above the telescope permits this target camera to view the LED. The images from this camera are useful for verifying tip/tilt motion and for viewing any motion of the RF secondary during a track. Actuators are controlled and images collected using a remote computer through a local-area network (LAN), which extends from the RF primary into a local control room in the antenna. A separate report on the details of the mirror assembly and actuator system is planned.

Here we focus on the focal plane assembly, depicted in Figure 4. The aluminum enclosure is visible just left of center in the image. The enclosure is mounted to the structure that supports the large RF secondary. Light enters through the black tube, which serves as a baffle, visible in the image. The dimensions of the enclosure are approximately 32″ × 24″ × 14″ and the overall assembly weighs approximately 160 lb. Adjustments to the vertical position of the assembly relative to the primary surface are accomplished by controlling a stepper-motor-driven Nook precision linear actuator. Image data are collected and the linear stage is controlled using a remote computer through a LAN that extends from the RF secondary into a local control room in the antenna. The details of this focal plane assembly are the subject of the remainder of this article. This second-generation assembly replaces an earlier, much simpler assembly, operated in the field over the last several years at DSS-13.

Figure 4. Focal plane assembly mounted off RF secondary.

II. Focal Plane Assembly

The optical layout of the focal plane assembly is depicted in Figure 5. Light from the two mirror segments enters through the baffle, which is mounted to the enclosure, and immediately passes through a long-pass filter at 800 nm. This filter is mounted on the baffle. The remainder of the components are mounted to a stiff optical plate/bench. This plate is, in turn, mounted directly to the mounting structure, while the enclosure is floating, providing

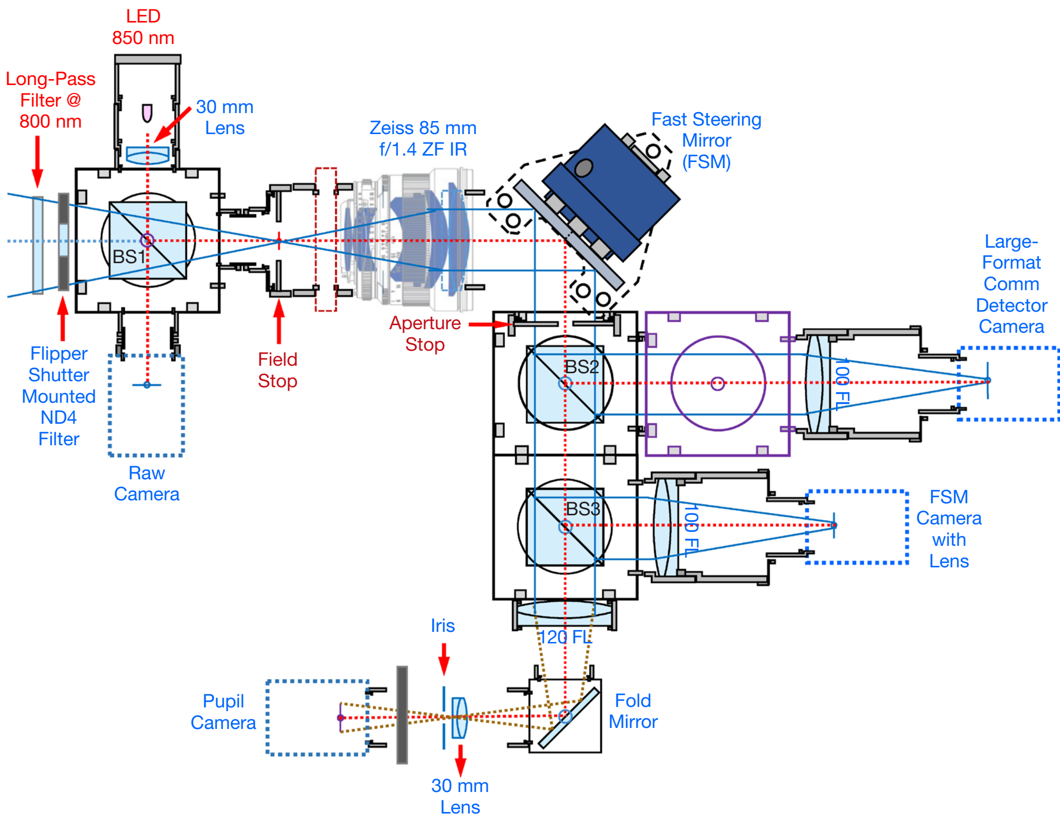

Figure 5. Optical layout of the focal plane assembly.

no structural support to the optics. After the light enters the baffle, it passes through the shutter, which is an ND4 filter mounted on an actuated flip stage. This shutter is normally in the closed position to minimize dust entering the assembly and flipped out for observations. It is controlled through a remote computer. After passing through a 50/50 beam splitter (BS1 in Figure 5), half the light enters the raw camera and lens, and half passes on to the upstream optics. The raw camera views the raw focal plane image prior to encountering the FSM. This camera, as well as the FSM camera and pupil camera, is a Basler acA645-100gm camera with 659 × 494 pixels,[1] which provides a field of view of approximately 450 × 350 microradians (μrad) on the sky. The fourth port of the beam splitter is used to inject a signal from an 850-nm LED into the system. This source is used to check out the system's operation independent of an astronomical source. It is remotely controlled on/off via computer.

A field stop is placed at the mirror segment focus and then the light is collimated using a Zeiss 85-mm f/1.4 ZF IR lens.[2] The light then passes through a rectangular aperture stop (see Figure 6). This stop limits stray light, admitting light only from a region slightly larger than the two hexagonal segments. Next, the collimated light passes through the FSM and on to the remaining components. The FSM system is described in detail in the next section. The next beam splitter, BS2, directs half the remaining light to a lens and large-format Basler camera that acts as a surrogate for the communications detector. This camera, an acA2040-

[1] http://www.baslerweb.com

[2] http://www.zeiss.com

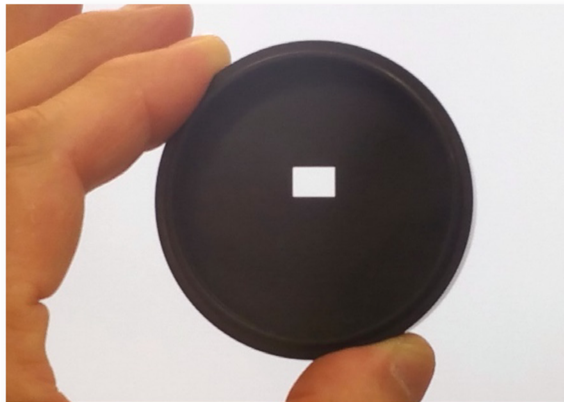

Figure 6. Custom rectangular aperture stop.

25gm camera,[3] has 2048 × 2048 pixels, which corresponds to a field of view of approximately 800 × 800 μrad on the sky. An additional beam splitter housing is included in this path to allow for future expansion of the system.

The remaining 50 percent of the light passes on to a final beam splitter, BS3, where half is directed to the FSM camera and the rest is passed on to the pupil camera system. The pupil camera portion consists of a 120-mm focal length lens, fold mirror, 30-mm lens, a remote-controlled variable iris, and the pupil camera itself. This system, which images the primary segments, is described in detail in an upcoming section.

Figure 7 shows the bulk of actual hardware, mounted on the optical plate, prior to placement in the enclosure. In addition to this optical component layer, there is an additional layer for power distribution. Not all LAN hardware, hubs, and cabling are depicted in this photo. Besides the components described above, this photo shows some added elements used during testing of the assembly at JPL. These include an additional beam splitter and test source at the input of the assembly. Light from this test source is directed to the segments by the beam splitter and retroreflected back into the optical during a test of the overall system. In the next two sections, we describe the FSM and pupil camera assemblies.

III. Fast Steering Mirror System

All optical ground stations are likely to suffer from low-frequency disturbances that adversely affect the overall pointing of the ground station. These disturbances will cause the focal plane spot to wander, and potentially drift off of the high-speed communications detector. As long as these disturbances are sufficiently slow, one may integrate the photons collected by the detector to determine a time-averaged displacement of the spot, and correct for this effect with a steering mirror. As mentioned above, a FSM system was included in the DSS-13 demonstration.

---

[3] http://www.baslerweb.com

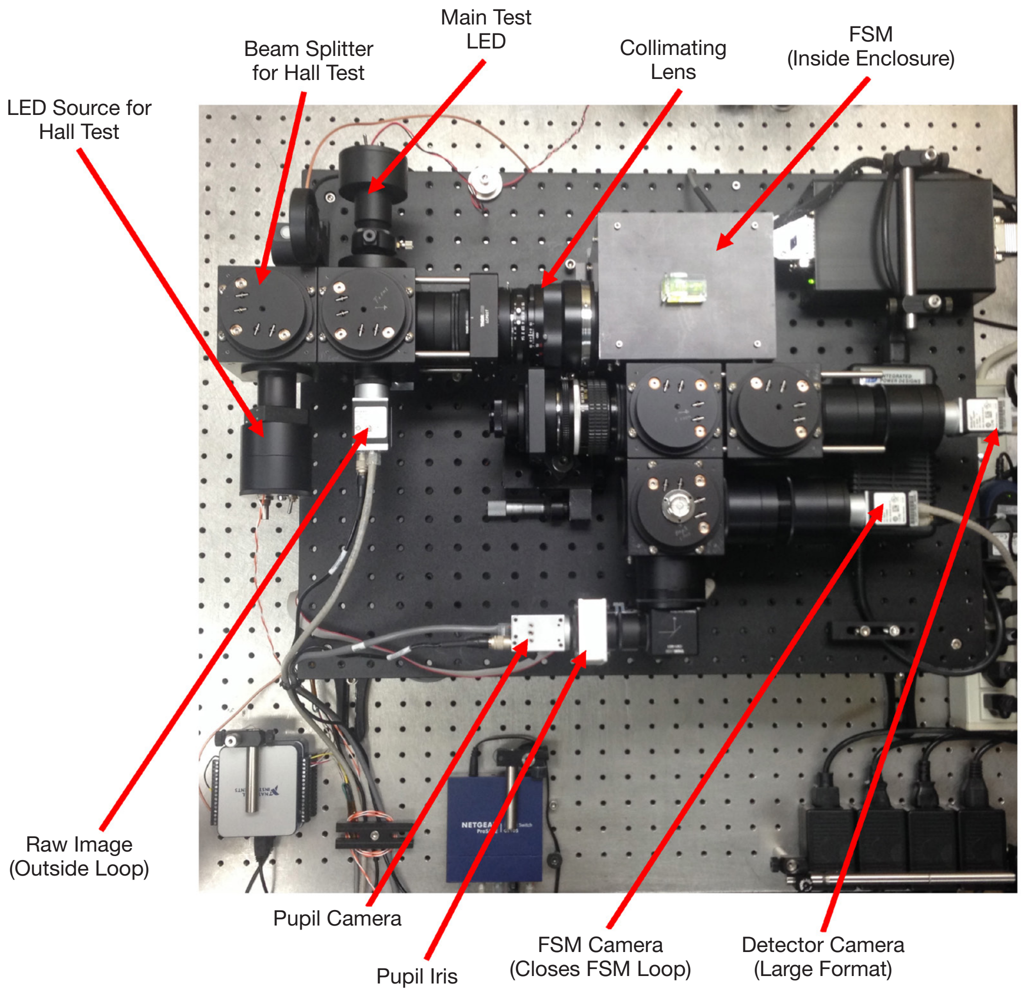

Figure 7. Photo of the focal plane assembly prior to addition of upper power layer.

The demonstration system suffers from two main effects that can be used to demonstrate the effectiveness of the FSM. The first is long-term drift of the RF antenna pointing. While this drift is not a factor for RF communications since it is small relative to the beamwidth of the antenna, which is 16 mdeg or 275 μrad at its highest frequency of operation, 32 GHz. This drift is on the order of 10 times the expected capture area of the communications detector. The accumulated drift depends on the quality of the RF pointing model but typically would take many minutes to build up to unsatisfactory levels and is easily corrected by the FSM. The corrections sent to the FSM can be monitored and used to improve future pointing models as well.

A second factor that can be corrected for using the FSM would be any structural resonances that fall within its bandwidth. On DSS-13, the primary effect of this type is wind-induced excitation of the first mode of the secondary support structure. This is the lowest resonant mode of the antenna system. We have observed the effect of this mode in preliminary experiments, particularly with wind speeds greater than 30 mph. Figure 8 shows the results of a structural analysis of the antenna, and depicts the nature of this first resonant mode. The frequency of the mode is 2.38 Hz, and the motion is a twisting of the secondary support about its center line. Since the focal plane assembly is mounted off-axis, this twisting motion couples into the focal plane, disturbing the location of the spot.

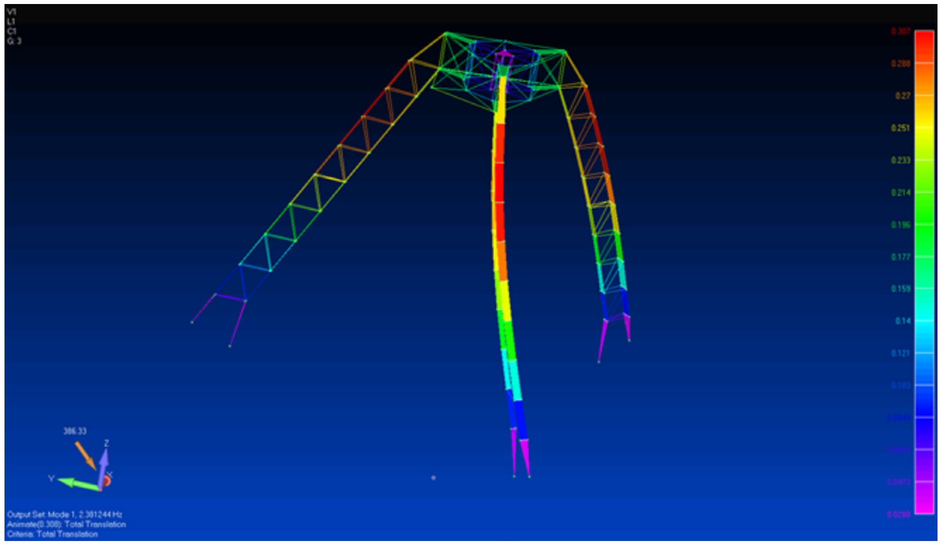

Figure 8. Resonance of the secondary support structure.

Figure 9 shows the measured spectrum of the spot centroid during a windy track at DSS-13. The black curve is a spectrum of the azimuthal spot motion and the red curve is the radial motion. As expected, the motion is nearly purely radial from the twist, and the resonant frequency is quite close to the predicted value of 2.38 Hz. These data were collected using the target camera on the primary surface, described earlier, when viewing the LED on the front of the camera box.

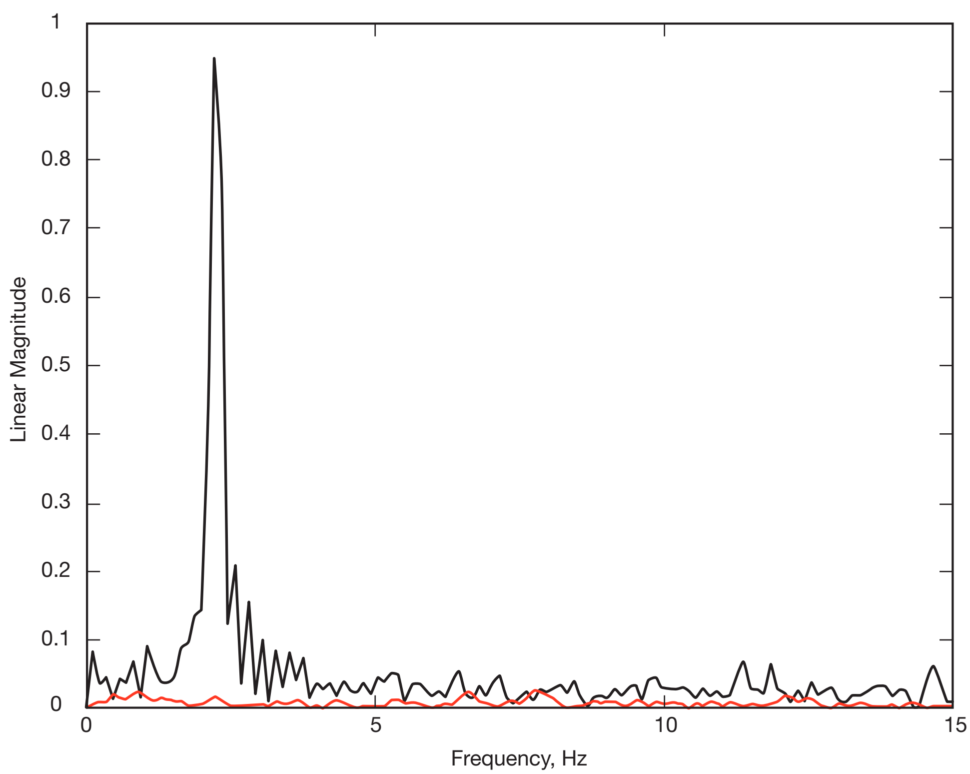

Figure 9. Measured resonance of the secondary support structure.

As shown earlier in the figures of Section II, the FSM system consists of the FSM itself, the FSM camera to collect the images, and a computer to close the loop. The FSM is depicted in Figure 10, it is from Optics in Motion, OIM202.3.[4] It has a 2″ × 3″ clear area, a 400-Hz, 3-dB bandwidth, and a range of ±1.5 deg. Control is via two ±10 V analog signals, one for each axis.

Figure 10. Fast steering mirror.

A National Instruments CompactRIO (reconfigurable IO modules) controller,[5] shown in Figure 11, is used to close the FSM loop. The controller reads the images from the Basler FSM camera, computes the centroid of the image, and sends voltage updates to the FSM to move the image to the center of the focal plane. This controller resides in the camera box enclosure and is independent of the main computers controlling the other cameras and actuators. Images, centroid data, and FSM voltages are made available to the control computers by the CompactRIO using a buffer system, which does not adversely affect the bandwidth of the FSM loop. The loop is engaged and disengaged using a remote computer communicating directly with the CompactRIO.

The centroid of the image spot is calculated using a weighted mean of the thresholded image. The camera integration time is set no higher than the loop time (10 ms) and the camera gain then adjusted to have the maximum spot intensity below saturation. The image threshold is set to only have the pixels around the image visible with the remaining pixels set to zero. This not only reduces the centroid error from background noise, but also accelerates the centroid processing time.

[4] http://www.opticsinmotion.net/

[5] http://www.ni.com/compactrio/

Figure 11. CRIO 9030 controller.

The current camera could not deliver a frame read time of less than 10 ms unless a subframe of the image with fewer pixels was used (in this case, 100×100 pixels). While this limits the field of view of the FSM channel, it does not create any performance issues since the other optical channels with a much wider field can bring the spot in. Once the FSM loop is engaged, there is sufficient field to always see the spot.

The control loop design used a straightforward feedback scheme consisting of the integral of the centroid and the double integral of the centroid, each with an adjustable gain. The first integral acts as a proportional feedback term to deal with dynamic motions of the image, while the second integral acts as an integral term to bring the spot to the desired location on the image plane.

Figure 12 shows the frequency response of the FSM system measured in the laboratory. The two curves, red and black, are the responses in the two axes of the FSM. As expected, they are essentially identical. As shown in the plot, the loop gives approximately 10 dB suppression of disturbances around the 2.4-Hz resonant frequency of the secondary structure.

The sampling rate of the camera limits the loop time and hence the bandwidth of the control loop. The current FSM has an effective bandwidth of a few hundred hertz and this would be the ultimate limit. A faster camera or other sensor like a quad cell would increase the bandwidth.

No attempt to shape the loop in order to increase the gain at specific frequency bands was made. This could be a simpler means of improving performance if most of the disturbances are below 10 Hz. For example, since the main source of disturbance is a resonance near 2.4 Hz, the introduction (digitally in the software) of a tuned resonant gain filter could dramatically increase the gain of the servo around the resonant peak and improve the rejection of the introduced noise.

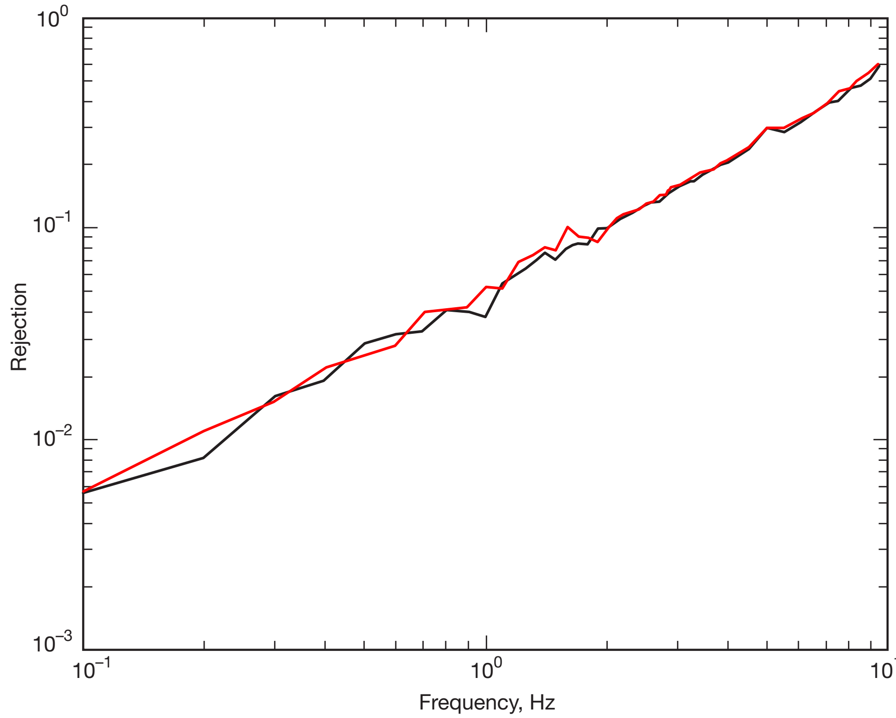

Figure 12. Measured response of the FSM loop.

IV. Pupil Camera

Any operational optical ground station is likely to comprise a number of primary mirror segments. These segments must be aligned initially and then this alignment must be maintained throughout a complete track. Initial alignment may be accomplished in a number of ways, including a pupil camera system, which was implemented in this demonstrator. We describe this system in some detail in this section. Active alignment of the segments throughout a track is likely to involve an edge-sensor system. The next-generation segment system is envisioned to have seven segments and a demonstration of edge sensing.

The basic operational principles of the pupil camera system are depicted in Figure 13. A portion of the incoming light from the segments is directed toward a lens and the pupil camera. The system is focused such that an image of the segments forms on the camera focal plane. An iris with a variable aperture size is placed either just before or after the lens. For a well-pointed segment, such as the rightmost (red) one in the diagram, all the light passes through the iris. As a consequence, the segment appears fully illuminated in the pupil camera image. On the other hand, if the segment is mis-pointed such as the one on the left (green), part of the light is blocked by the iris and the segment appears only partially illuminated, in this case only on the leftmost edge.

The image on the right half of Figure 13 is clearly a function of the iris size and the pointing error of the segment. For a large iris opening, large pointing errors in any segment go undetected, while for a small opening all segments except those with excellent pointing will appear dark. Figure 14 shows a simulation of the pupil camera system for a segment

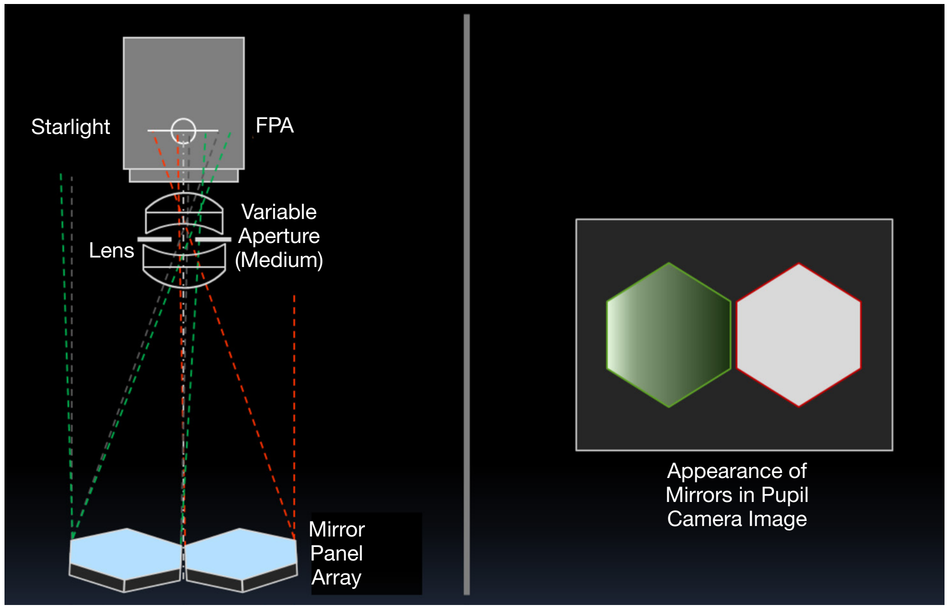

Figure 13. Basic operation of the pupil camera system.

with a pointing error of 100 μrad. The figure indicates the X and Y centroids of the image as the iris is swept from totally open (center of plot) to totally closed (tip of each branch). Each branch corresponds to a different orientation of the 100 μrad pointing error. For the remainder of this discussion, we focus on the 30-deg branch highlighted in the figure. On the right side are images corresponding to three different iris openings, and hence points on the branch. As the iris closes, the segment image becomes clipped and the centroid moves, in this case along a 30-deg line. At the edge of the branch, the iris closes far enough that no light from the segment passes to the pupil camera.

The absolute value of the segment pointing error is determined by the iris opening for which the segment image vanishes. The direction of the error is determined by tracking the motion of the centroid in the segment's image as the iris closes. While illustrated here for a single segment, the pointing errors of all segments may be computed simultaneously from one set of pupil images taken for various iris apertures. This is one key advantage of the pupil camera system.

The most important component in the pupil camera system is the iris. Important factors are the minimum iris opening, which determines the smallest segment tip/tilt that can be detected; and the maximum opening, which determines the capture range of the system. These essentially determine how good the initial segment pointing needs to be for the system to be able to see the segment at all. The aperture step size could be a factor as well but most of the commercial single-stage irises we considered were acceptable. While an iris that closes completely is desirable, all the commercial models investigated accomplished this by placing two sets of blades in close proximity. Simulations show that such a dual-iris arrangement causes significant confusion in the results and is not desirable.

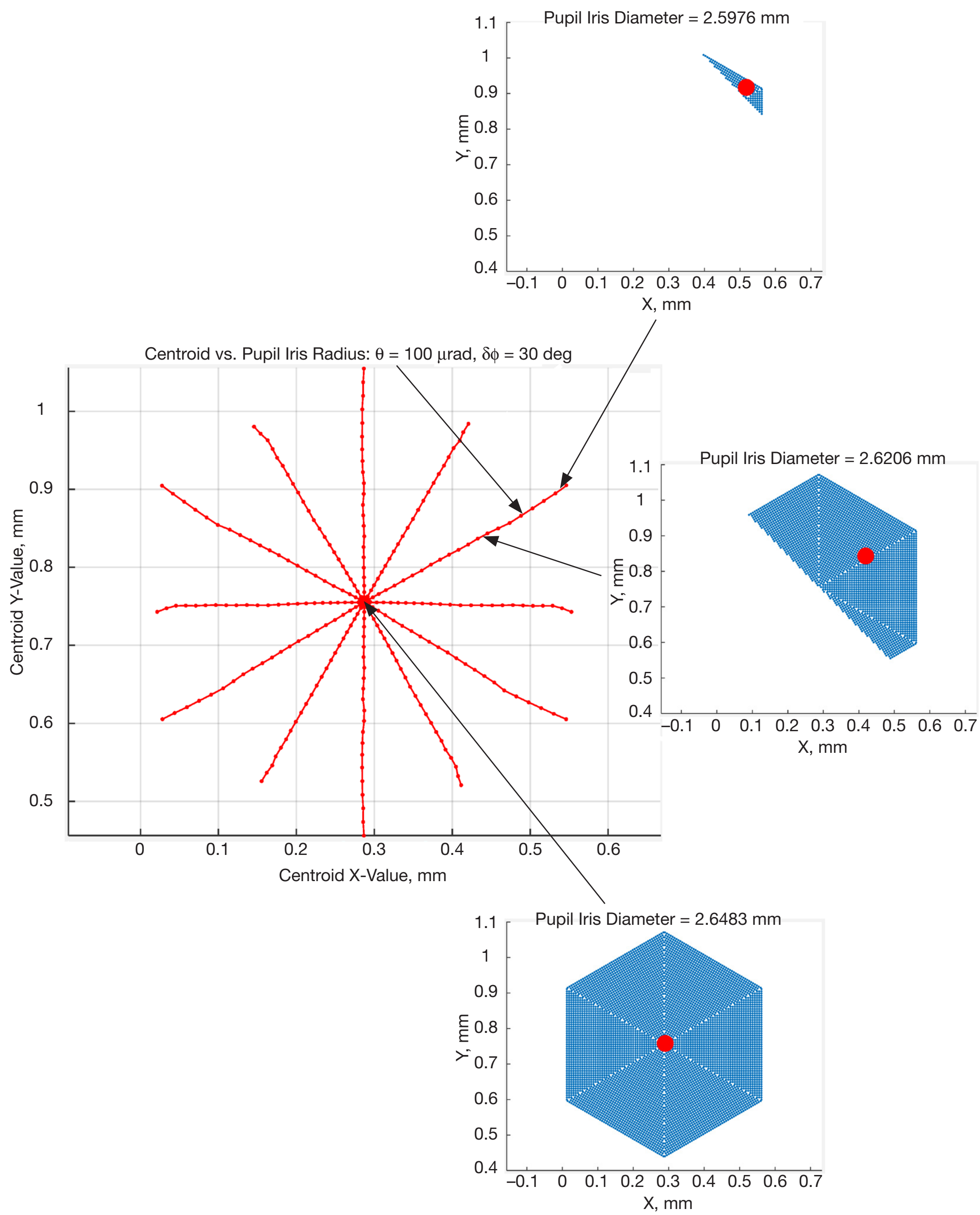

Figure 14. Quantifying the pupil camera image.

For this demonstration, we employed a motorized pupil iris from Pacific Laser Equipment, model number IMS-20-1.[6] The iris spans diameters of 1 to 20 mm with a resolution of approximately 1500 steps/mm. In the current system, these limits result in a maximum detectable pointing error of 37.5 μrad, and a maximum of 750 μrad. A photograph of the iris is shown in Figure 15.

We have elected to control the pupil camera and iris through the CompactRIO as well. An interface to the system for setting parameters and receiving images is presented to the remote computer by the RIO.

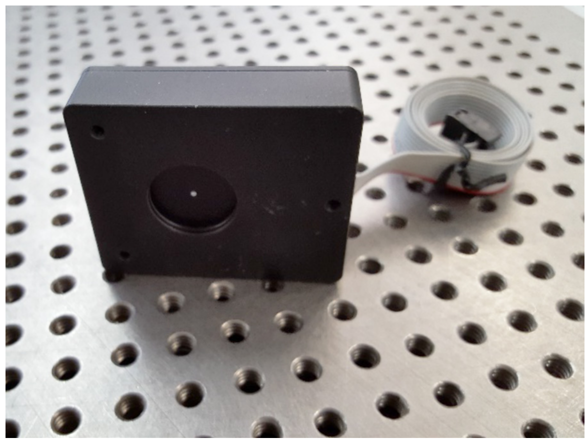

Figure 15. Motorized pupil iris.

Laboratory testing of the pupil camera system has verified its basic functionality and limits. Primary testing will take place in the field over the next few months. Of course, the pristine results depicted in Figure 13 will never occur in a practical, realized, system. In particular, imperfections in the mirrors will scatter light near the pupil iris. This light will also be clipped by the iris and the corresponding region on the mirror will become dim prematurely. This phenomena, which is similar to what occurs in a knife-edge test of a mirror, complicates the algorithm used to deduce pointing error and direction from the swept iris images. Development of practical algorithms and demonstration of their use in a real-world environment is one goal of the demonstrator experiments.

V. Focus Adjustment

As mentioned earlier, the entire focal plane assembly and enclosure are mounted on a linear stage, allowing a focus adjustment of the system. The stage is based on the Nook 252-18-L18/1000-0250 SRT RA linear slide,[7] shown in Figure 16. The slide has a range of ±2.25 in., with a ball screw pitch of 0.25 in. per revolution and a lead accuracy of ±.004 in./ft. The linear slide is driven by an Applied Motion stepper motor, model number HW23-601, and a ST10-IP-EN microstep drive controller. The motor and controller deliver 25,000

[6] http://plequipment.com/

[7] http://www.nookindustries.com

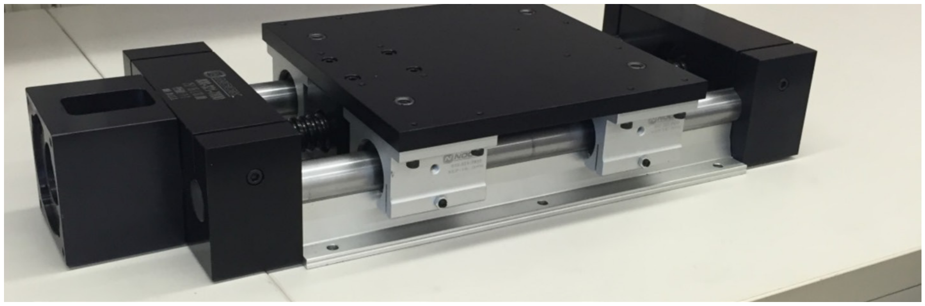

Figure 16. Linear stage for focus adjustment.

microsteps per revolution. The final result is a resolution of 0.254 microns per step, greatly exceeding any focus resolution requirement. The linear stage is controlled through a remote computer and Labview. Expectations are that focus will not need to be adjusted beyond the one-time adjustment done at installation.

VI. Overall Control

All components in the demonstration, including those on the primary surface, are controlled through a LAN. A block diagram describing the interconnection of the components in the focal plane assembly is shown in Figure 17. Two independent LAN cables run from the local antenna control room to the assembly mounted on the secondary. One is connected directly to the CompactRIO while the other connects to a hub in the enclosure. The CompactRIO is connected directly to the FSM camera via a local LAN cable. It is also connected to the FSM through two analog voltage cables, to the pupil iris through servo control cables, and finally to the shutter through a simple cable carrying transistor–transistor logic (TTL) signals. The hub connects the remaining cameras and linear stage to the control room through the second LAN cable. All control software is implemented using Labview, both for the focal plane assembly and the equipment on the RF primary.

VII. First-Light Results

First operation of the new focal plane assembly took place in late August 2016, using the astronomical source Arcturus. Small differences in the position of the new focal plane assembly relative to the first-generation system demanded small adjustments to the segment actuators in order to bring the focal plane spots onto the imaging camera. These adjustments were quite small, on the order of tenths of a millimeter, even after a span of over one year since the last operation of the system. Next the linear stage was adjusted to bring the spots into best focus.

After focus was achieved, three of the segment actuators were adjusted to bring one of the spots to the center of the focal plane. The top two panes of Figure 18 show the two spots in the focal plane (left) and the corresponding pupil image (right). Note that only the segment producing the spot falling at the center of the image plane inside the red circle appears illu-

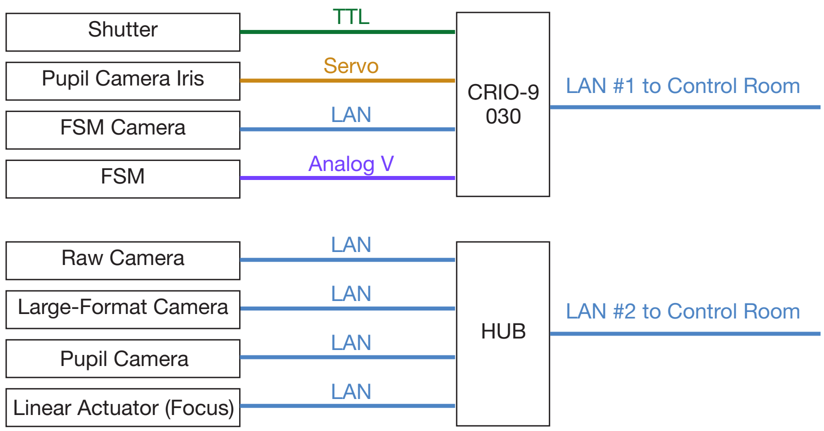

Figure 17. Measured response of the FSM loop.

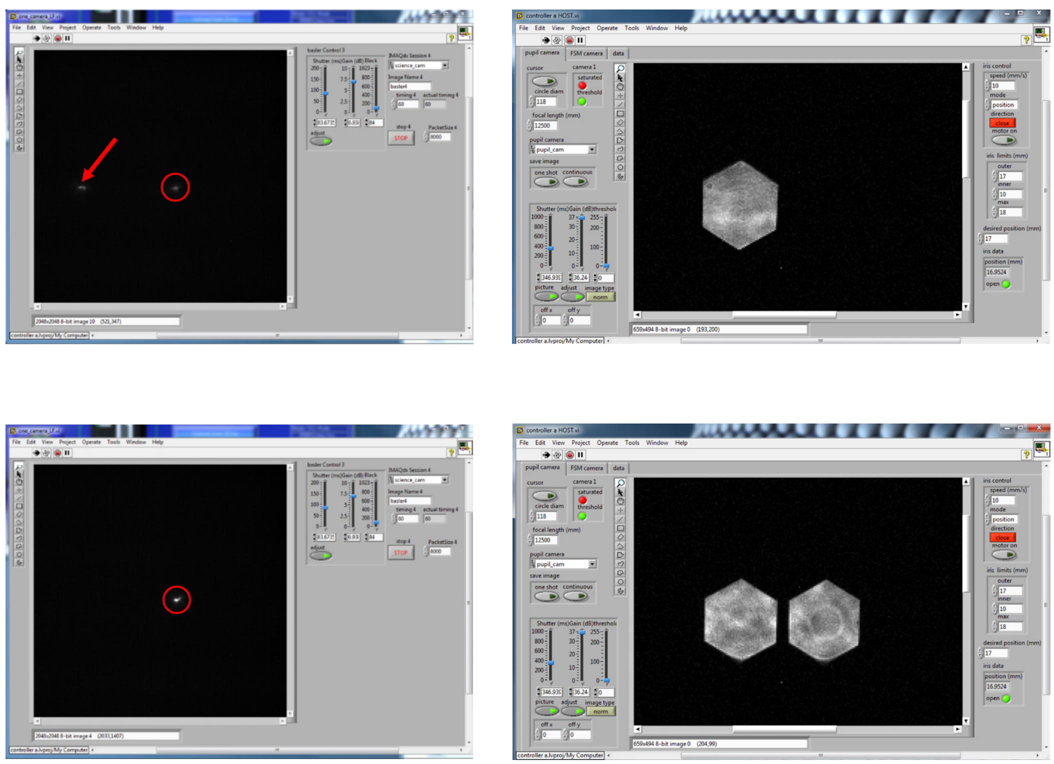

Figure 18. Top: focal plane (left) and pupil camera (right) images for one mirror on-point. Bottom: focal plane (left) and pupil camera (right) images for both mirrors on-point.

minated in the pupil image. Adjustment of the final two actuators merges the second spot with the first as shown in the lower left pane of the figure. As expected, the pupil camera image confirms that both segments are illuminated properly and on-point.

This initial experiment determined optimum focus, and confirmed basic operation of the pupil and imaging camera systems. Future experiments will demonstrate operation of the FSM in windy conditions and collect data on composite focal plane spot sizes for a wide range of source locations and tracking conditions. We also intend to develop an all-sky pointing model for the system and document its accuracy and repeatability. As mentioned above, we will also quantify the performance of the pupil camera system and develop algorithms to use its data to align the segments. It is also important to demonstrate all the relevant features of the system in the daytime as well as in dark-sky conditions.

VIII. Conclusions

The second-generation focal plane assembly fielded in the RF/optical demonstration has been described. The system includes both a fast steering mirror system and a pupil camera system for segment alignment. Initial operation of the system has verified basic functionality of all cameras, including the pupil camera system. Many experiments will be conducted over the coming months to quantify its operation in both daytime and nighttime conditions. Future reports will document these results. A future upgrade of the two-segment mirror system to a seven-segment system with edge sensing is currently under development and this will also be the subject of a future report.

Acknowledgments

The authors would like to acknowledge major contributions from Jeff Charles, who originally designed the focal plane assembly and provided considerable guidance during its fabrication, test, and initial operation on the antenna. We also acknowledge Troy Torrez, who computed the subreflector support structure's natural frequency.

References

[1] H. Hemmati, ed., *Deep Space Optical Communications*, JPL Deep Space Communications and Navigation Systems Center of Excellence (DESCANSO) Book Series, Deep Space Communications and Navigation Series, vol. 7, Jet Propulsion Laboratory, Pasadena, California, October 2005.
http://descanso.jpl.nasa.gov/monograph/series7/Descanso_7_Full_Version+.pdf

[2] A. Biswas, J. M. Kovalik, M. Srinivasan, M. Shaw, S. Piazzolla, et al., "Deep Space Laser Communications," Proceedings of SPIE, vol. 9739*, Free-Space Laser Communication and Atmospheric Propagation XXVIII*, 97390Q, March 15, 2016.

[3] K. S. Shaik and W. L. Kerr, "A Ten-Meter Optical Telescope for Deep-Space Communications," Proceedings of SPIE, vol. 1236, *Advanced Technology Optical Telescopes IV*, pp. 347–350, July 1, 1990.

[4] M. Britcliffe, D. Hoppe, W. Roberts, and N. Page, "A Ten-Meter Ground-Station Telescope for Deep-Space Optical Communications: A Preliminary Design," *The Interplanetary Network Progress Report*, vol. 42-147, Jet Propulsion Laboratory, Pasadena, California, July-September 2001, pp. 1–17, November 15, 2001.
http://ipnpr.jpl.nasa.gov/progress_report/42-147/147G.pdf

[5] J. Breidenthal, H. Xie, and L. Clare, "Optical Ground Segment Performance Summary," *The Interplanetary Network Progress Report*, vol. 42-205, Jet Propulsion Laboratory, Pasadena, California, pp. 1–17, May 15, 2016.
http://ipnpr.jpl.nasa.gov/progress_report/42-205/205A.pdf

[6] J. Breidenthal and D. Abraham, "Design Reference Missions for Deep-Space Optical Communication," *The Interplanetary Network Progress Report*, vol. 42-205, Jet Propulsion Laboratory, Pasadena, California, pp. 1–19, May 15, 2016.
http://ipnpr.jpl.nasa.gov/progress_report/42-205/205B.pdf

[7] H. Xie, D. Heckman, and J. Breidenthal, "Link Characterization for Deep-Space Optical Communications," *The Interplanetary Network Progress Report*, vol. 42-205, Jet Propulsion Laboratory, Pasadena, California, pp. 1–33, May 15, 2016.
http://ipnpr.jpl.nasa.gov/progress_report/42-205/205D.pdf

[8] L. Clare, G. Miles, and J. Breidenthal, "Optical Communications Performance with Realistic Weather and Automated Repeat Query," *The Interplanetary Network Progress Report*, vol. 42-205, Jet Propulsion Laboratory, Pasadena, California, pp. 1–19, May 15, 2016.
http://ipnpr.jpl.nasa.gov/progress_report/42-205/205C.pdf

[9] J. R. Charles, D. J. Hoppe, and A. Sehic, "Hybrid RF/Optical Communication Terminal with Spherical Primary Optics for Optical Reception," *Space Optical Systems and Applications (ICSOS), 2011 International Conference*, pp. 171–179, May 11–13, 2011.

[10] A. Carrasco-Casado, J. M. Sánchez-Pena, and R. Vergaz, "CTA Telescopes as Deep-Space Lasercom Ground Receivers," *IEEE Photonics Journal*, vol. 7, no. 6, December 2015.

[11] W. A. Imbriale, *Large Antennas of the Deep Space Network*, JPL Deep Space Communications and Navigation Systems Center of Excellence (DESCANSO) Book Series, Deep Space Communications and Navigation Series, vol. 4, Jet Propulsion Laboratory, Pasadena, California, February 2002.
http://descanso.jpl.nasa.gov/monograph/series4/Descanso_Mono4_web.pdf